Quantification of myosin distribution predicts global morphogenetic flow in the fly embryo

SJ Streichan[1,2], MF Lefebvre[3], N Noll[2], EF Wieschaus[3,4], and BI Shraiman[1,2]

[1,2] *Kavli Institute for Theoretical Physics, University of California, Santa Barbara, USA*
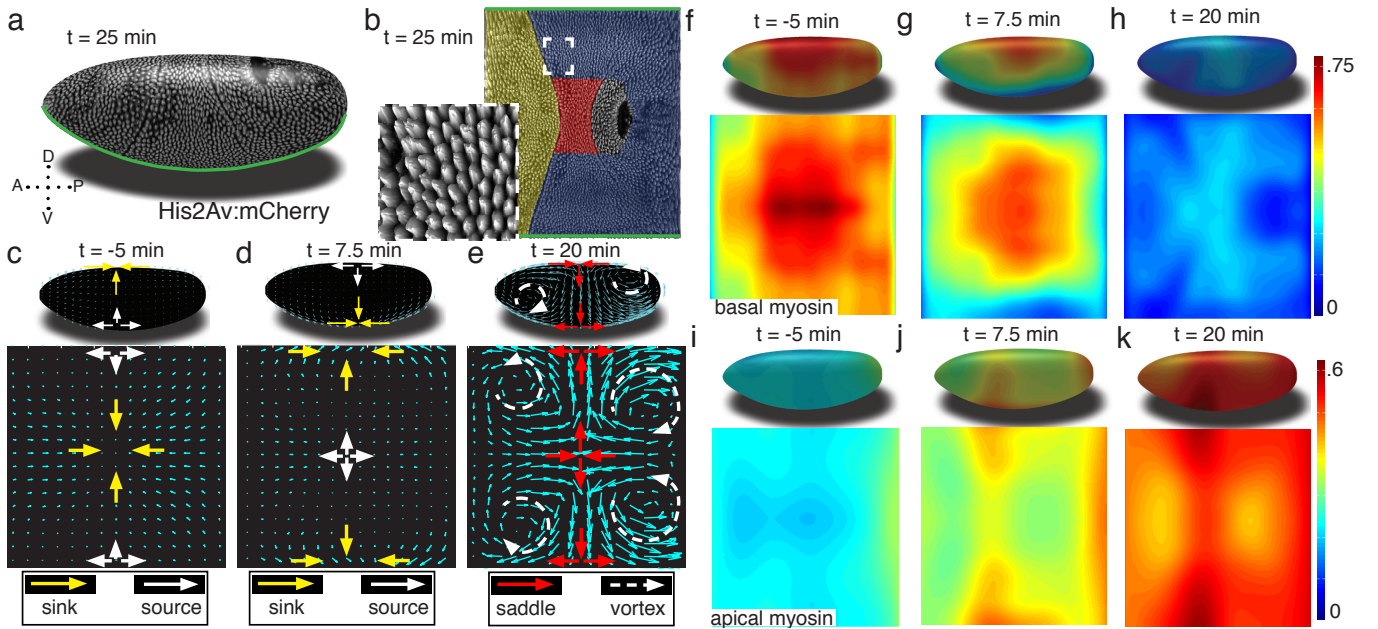[2] *Department of Physics, University of California, Santa Barbara, USA and*
[3] *Department of Molecular Biology,* [4] *Howard Hughes Medical Institute, Princeton University, USA*

During embryogenesis tissue layers continuously rearrange and fold into specific shapes. Developmental biology has identified the spatio-temporal patterns of gene expression and cytoskeletal regulation that underlie such tissue dynamics on the local level, but how actions of multiple domains of distinct cell types coordinate to remodel tissues at the organ scale remains unclear. Here we combine *in toto* light-sheet microscopy with automated segmentation-free image analysis and physical modeling to quantitatively investigate the link between kinetics of global tissue transformations and patterns of force generation during *Drosophila* gastrulation. We find that embryo-scale shape changes are represented by a temporal sequence of three simple flow field configurations. Each phase is accompanied by a characteristic spatial distribution of myosin molecular motors, which we quantify in terms of a coarse-grained 'myosin tensor' that captures both myosin concentration and anisotropy. Our model assumes that tissue flow is driven by stress proportional to the myosin tensor, and is effectively visco-elastic with two parameters that control the 'irrotational' and 'divergence-less' components of the flow. With a total of just three global parameters, this model achieves up to 90% agreement between predicted and measured flow pattern. The analysis uncovers the importance of a) spatial modulation of myosin distribution and b) the long-range spreading of its effect due to mechanical interaction of cells. In particular, we find that transition to the germband extension phase of the flow is associated with the onset of effective areal incompressibility of the epithelium, which makes the relation of the flow and myosin forcing strongly non-local. Our quantitative analysis also revealed a new function for basal myosin in generating a dorsally directed flow and, combined with the mutant analysis, identified an unconventional control mechanism of this function through *twist* dependent reduction of basal myosin levels on the ventral side. We conclude that understanding morphogenetic flow requires a fundamentally global perspective.

During *Drosophila* gastrulation, dynamic reconfiguration of the cytoskeleton of mechanically coupled cells facilitates tissue rearrangements(Bertet et al., 2004; Irvine and Wieschaus, 1994; Martin et al., 2009; Zallen and Wieschaus, 2004). Cell type specific behaviors have been associated with certain configurations of the force generating non-muscle myosin II(Martin et al., 2009; Zallen and Wieschaus, 2004). Yet, how multiple domains of different cell types contribute to global movements remains unclear(Blanchard et al., 2009; Butler et al., 2009; Lye et al., 2015). Debates on mechanical aspects of tissue transformations demonstrate the need for a multi-scale description of how physical stress coordinates molecular phenomena with global tissue flows(Collinet et al., 2015; Rauzi et al., 2015; Rickoll and Counce, 1980). Single cell analysis revealed complex mechanisms linking cell behavior to flow(Bosveld et al., 2012; Etournay et al., 2015). However, the mesoscopic organization(Blankenship et al., 2006; Martin et al., 2009) and its capacity to generate physical stresses suggest that tissue flows may be more naturally understood in terms of myosin generated stresses across the entire epithelia rather than single-cell behavior. Current technology falls short of directly measuring stresses at the organismal level(Brodland et al., 2010), thus we use physical modeling to express stress in terms of quantitative measurements of myosin activation patterns and compare quantitative predictions to quantifications of tissue flows.

With this in mind, we generated a pipeline that combines *in toto* light sheet microscopy (Krzic et al., 2012; Tomer et al., 2012) (Fig 1a), tissue cartography(Heemskerk and Streichan, 2015) (Fig 1b), and segmentation-free anisotropy detection to quantify global tissue flows, and myosin activation patterns. We find that tissue remodeling during *Drosophila* gastrulation is characterized by three simple flow field configurations (Fig 1c-e). The earliest flows start well before the ventral furrow (VF) forms, and are characterized by a dorsal sink and ventral source (Fig 1c). In contrast to the VF, no cells are internalized during this flow, but rather cells reduce cross section on the dorsal side (Fig S1c). As the VF forms, source and sink swap sides and a large group of cells internalize on the ventral side, as mesoderm precursors leave the surface of the blastoderm (Fig 1d). During germband extension (GBE), the flow pattern exhibits two saddles arranged on the dorsal and ventral sides as well as four vortices, two in the posterior and two in the anterior end (Fig 1e). Each of the three flow fields is accompanied by a typical spatial myosin configuration. The pre-VF flow associates with basal myosin that exhibits a pronounced Dorso Ventral (DV) symmetry breaking(Polyakov et al., 2014; Sokac and Wieschaus, 2008; Warn et al., 1980), with high levels of myosin on the dorsal and low levels on the ventral side (Fig 1f), while the apical pool appears homogeneous across the surface (Fig 1i). The basal pool remains
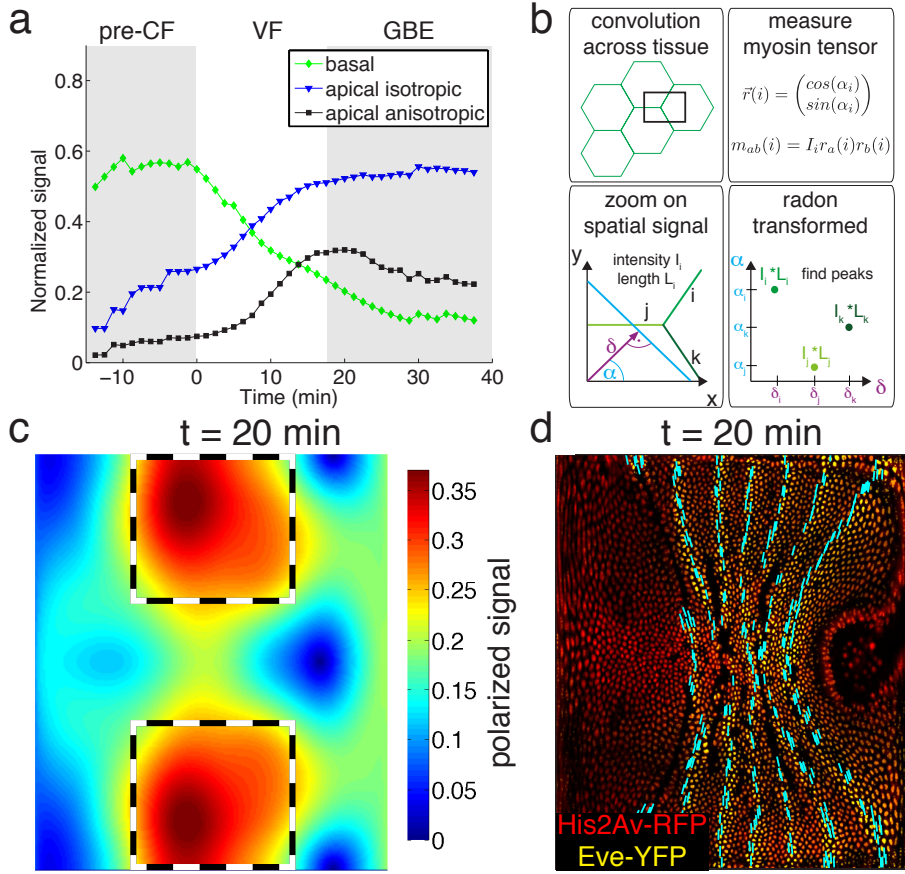
FIG. 1: Tissue deformations of *D. melanogaster* embryos during gastrulation, captured by three simple flow fields. (**a**) Stage 7 embryo labeled with His2Av:mCherry. Anterior is to the left, dorsal up. Time is chosen such that 0 min coincides with the first occurrence of the cephalic furrow (CF). (**b**) Thin sub-apical layer through embryo shown in (a), with prospective head, germband and amnioserosa color-coded. Anterior is left, posterior right, dorsal is in the center and ventral is on top and bottom. Inset shows zoom into anterior germband region. (**c-e**) Flow field on 2D projections for representative time points of the pre-Ventral Furrow (pre-VF) phase (c), Ventral Furrow (VF) phase (d), and germband phase (GBE) (e). Cyan arrows indicate tissue flow field. Bold arrows indicate flow field topology: sinks (yellow), sources (white), saddles (red) and vortices (dashed white). Insets show flow field on corresponding 3D surface. (**f-h**) Normalized myosin distribution on basal cell surface corresponding to times shown in (c-e). (**i-k**) As (f-h) except for isotropic pool on apical cell surface.

asymmetric during VF flow (Fig 1g), but the apical pool now also displays broken DV symmetry in reversed orientation (Fig 1j). The asymmetry on the apical surface becomes further pronounced in the GBE-phase (Fig 1h,k).

Global reconfigurations of myosin pools are a hallmark for transitions in flow field configuration (Fig 2a). Myosin is initially enriched in the basal pool, and as sink and source swap position, it begins to accumulate on the apical side. While the basal pool is isotropic, cortical myosin on the apical cell surface is known to polarize during convergent extension(Bertet et al., 2004; Zallen and Wieschaus, 2004). To quantify this effect at the tissue level, we developed an automated segmentation-free anisotropy detection algorithm (Fig 2b). Available methods for anisotropy detection mostly operate at the single cell level and construct a nematic tensor by integrating signal intensities along cell outlines(Aigouy et al., 2010). At the organismal scale membrane segmentation is costly, and often fails to define closed outlines of cells using only a polarized membrane marker. We overcome the need for fiduciary markers that increase experimental complexity by shifting the perspective to cell edges and using the Radon transform to implement a robust and rapid segmentation-free algorithm for detecting course-grained anisotropy (Fig 2b)(Radon, 1917).

Radon transforms integrate signal along lines of given orientation and normal distance from the origin. In this way, edges are mapped to peaks that reflect the total intensity along the length of an edge (Fig 2b) (see SI for detail). Edge orientation and average intensity are summarized in a nematic myosin tensor (Fig 2b). By averaging the resulting tensors in a given region, we obtain a quantitative description of local tissue anisotropy that reflects the intensity-weighted average of cell edges. The anisotropic signal in the apical pool starts out low, but increases from about 8 min corresponding to late stage 6 (Fig 2a). The anisotropy axis, readily computed by the eigenvectors of the myosin tensor, aligns well with local tangent to pair rule genes (Fig 2a,d). This is the expected result given that anisotropies are thought to be driven by the patterned juxtaposition of pair-rule gene expression(Zallen and Wieschaus, 2004). To relate myosin to stress, we assume signal intensity is proportional to myosin motor concentration and its local activity. The latter - pulling on cytoskeletal actin filaments - generates local force dipoles, which can be explicitly described in terms of local stress tensor (see SI for details)(Marchetti et al., 2013; Prost et al., 2015). On the coarse grained level, resulting stress would be defined by the activity weighted average over filament orientations and hence proportional to the myosin tensor as we define it (SI). The resulting force per unit area of
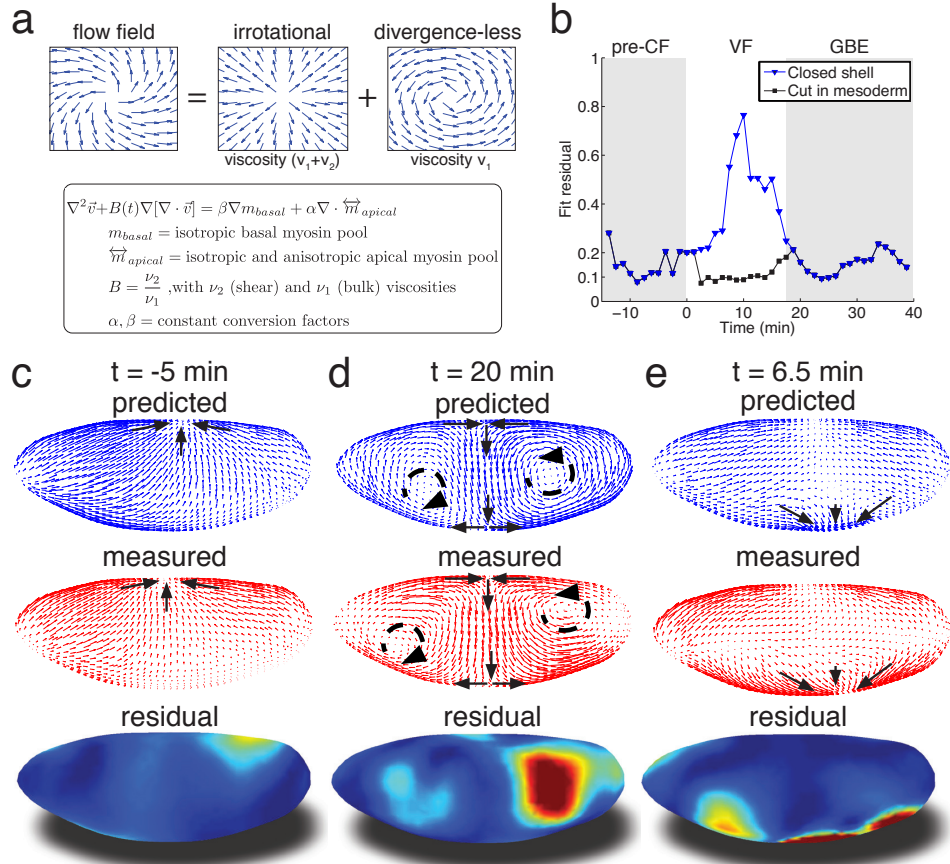
FIG. 2: Quantitative analysis of myosin distribution and anisotropy reveals transition across pools. (a) Normalized signal strength of basal, apical, and polarized pools over time in the lateral ectoderm (outlined as dashed box in c).(b) Automated extraction of polarization from images, and quantitative summary as nematic tensor. Top left box shows cell outlines in part of a tissue, and a region of interest (ROI), that moves across the tissue. Bottom left box shows zoom on spatial signal in ROI. Shades of green indicates potentially different intensities of lines i, j, k. Average intensity and length of lines in images are I and L. Radon transforms integrate signal along lines (cyan) of orientation α at normal-distance δ from the origin (purple). Bottom right inset shows sketch of radon-transformed signal. Note that lines are now peaks at angle α, and distance δ, of height $L * I$. Top right inset shows definition of unit vector with orientation of edge, contracted with itself and weighted by line average intensity to construct nematic tensor. (c) Magnitude of nematic on pullback (see SI for definition). Dashed box indicates region of interest used to compute time traces in a. (d) Eigen vectors of myosin tensor plotted in cyan over embryo labeled with His2Av-RFP (red), and eve-YFP (yellow). For simplicity only eigenvectors along eve stripes are shown.

the epithelial layer is then proportional to the divergence of the myosin tensor(Landau et al., 2012). Note that the isotropic component of the myosin distribution (observed both in the apical and the basal pool) also generates a force that is proportional to the gradient of the measured concentration intensity profile (Fig 1f-k).

To relate myosin generated stress to morphogenetic flow, we assume that on the mesoscopic scale tissue flow is governed by effective viscoelasticity which arises from the mechanical properties of the underlying cytoskeletal network within the two dimensional epithelial layer of cells. This model assumes that on short time scales tissues respond elastically to mechanical perturbations(Bambardekar et al., 2015), yet on longer time scales elastic stress is relaxed through active rearrangement of the cytoskeleton as cells adapt to the imposed deformation. On the longer time scale tissue dynamics can be described by a two-dimensional effective viscous flow equation with two effective viscosity parameters that (see model SI) are directly related to the two elastic constants: shear modulus (controlling 'sliding' of cells relative to each other) and the planar bulk modulus (controlling areal compression or dilation)(Marchetti et al., 2013; Martin et al., 1972; Prost et al., 2015) (Fig 3a). We note that effective viscosity spreads the impact of local forcing, generating a non-local response so the flow at any given point integrates the influence of forces acting all over the embryo. Inverting the equation using the finite element method, we obtain a quantitative prediction for the flow field generated by measured myosin localization patterns (see SI for details). Our model has only three global parameters: the ratio of effective viscosities, and the conversion factors relating normalized apical and
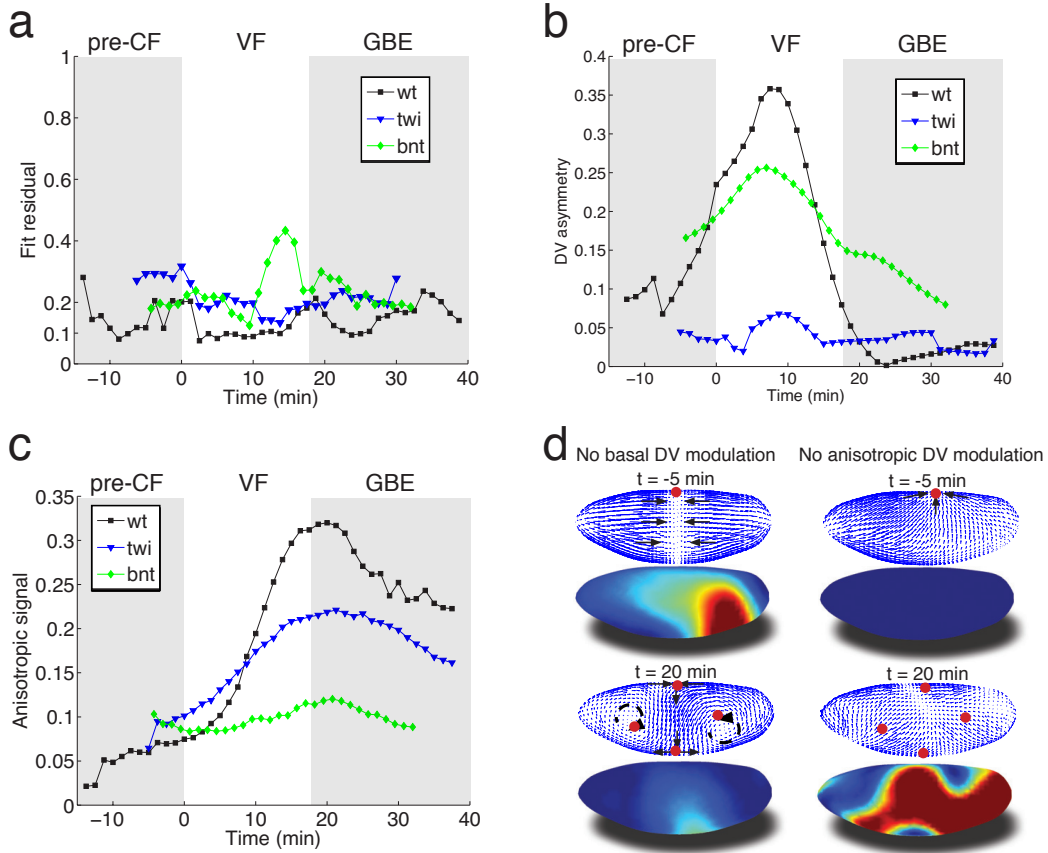
FIG. 3: **Biophysical model quantitatively predicts tissue flow based on quantitative measurements of myosin distribution.** (**a**) Proposed mathematical description of the flow parameterizes complex mechanics of cytoskeleton in terms of two effective viscosities: ν_1 which controls the divergence-less (i.e. circulatory) component of the flow and ν_2 which controls the irrotational (i.e. converging or diverging) component. The flow is driven by the force proportional to the divergence of the myosin tensor (see SI) on the right-hand-side of Eq. 3a. Because effective viscosity tends to suppress velocity differences of neighboring cells, the response to local forcing if felt globally, e.g. effect of a local myosin perturbation can result in local, but also non-local changes of the flow field. (**b**) Fit residual, comparing predicted flow field with measured flow field normalized for magnitude (see SI for detail) as a function of time. (**c-e**) From top to bottom spatial distribution of predicted (blue), measured (red) flow field, and residual (blue best agreement, red worst, on a scale from 0 to 1) for select time points.

basal myosin intensity to stress. To keep the model as simple as possible we do not allow spatial dependence of these parameters and keep conversion factors constant, leaving the ratio of viscosities as the only time-dependent global fitting parameter.

Even without spatial modulation of the parameters, the model achieves about 90% accurate description of the flow pattern before and after VF invagination (see Fig 3b). The main discrepancy of model predictions for pre-VF flow (see Fig 3c) is a displacement of sink and source positions along the AP axis by less than $30\mu m$. Prediction of GBE flow essentially agrees with measurements across the entire embryo, with the exception of a domain close to the vortices on the posterior end, due to a mismatch of fixed-point location (Fig 3d) (see SI for details). Remarkably our model is even able to correctly predict subtle differences between anterior and posterior fixed points along the DV axis (Fig 3d). Measured flow is first dominated by sources and sinks that disappear later during GBE, suggesting that before and during VF invagination cells are less resistant to surface area compression than during GBE. Indeed, quantitative comparison with an independently measured flow field (Fig 1c-e) shows that the ν_2/ν_1 ratio increases dramatically at the start of GBE phase (corresponding to the relative increase of the underlying 2D bulk modulus, see SI) resulting in effective incompressibility of apical surface of cells. Poor agreement during VF invagination is due to a significant fraction of cells internalizing and thus leaving the surface. To account for this effect, we extend the model to allow a 'cut' in the lattice along ventral midline with an imposed in-plane boundary force (perpendicular to the cut) representing the pulling effect of the VF (see SI for detail). This relatively simple extension allows to recover 90% accuracy (Fig 3be), illustrating how regional inhomogeneity associated with particular morphogenetic events could be quantitatively captured by suitable generalizations.

FIG. 4: **Mutant analysis reveals global modifications of myosin dynamics.** (**a**) Fit residual as in fig. 3b, for *twi*, and *bcd nos tsl* mutants, with WT reference. (**b**) Amplitude of basal myosin pool along DV axis for WT and mutants in (a). (**c**) Polarized apical myosin in mutants shown in (a) as function of time. (**d**) Theoretical comparison of DV constant basal pool (i.e. no gradient in DV direction) (left column), or DV constant anisotropic apical pool (i.e. no gradient in DV direction) (right column) with predicted flow based on full myosin tensor (compare to figure 3c,d respectively). Black arrows indicate flow field topology, and red dots the fixed point from prediction based off of full myosin tensor.

To evaluate the fit obtained in wild type embryos, we examined flows in mutant embryos in which the distribution of myosin is altered. Analysis based on tissue tectonics(Blanchard et al., 2009) has shown that strain rates in *twist* (*twi*) embryos, which lack the VF, exhibit slower kinetics compared to WT(Butler et al., 2009), however the cause of this remains a subject of debate(Butler et al., 2009; Collinet et al., 2015; Lye et al., 2015). We have quantified the flow field and myosin activity patterns in *twi* mutants, and find that our model is able to accurately predict the flow profiles (Fig 4a). During early flow phases - corresponding to times of pre-VF flow in WT - DV asymmetry of the basal myosin pool is strongly reduced in comparison to WT, as is tissue movement towards the dorsal pole (Fig 4b, SI, Fig S1). Moreover, anisotropy of the apical myosin pool increases at a slower rate as compared to WT. As previously reported for strain rates(Butler et al., 2009), this is most pronounced for the first 20 min (Fig 4c). In *bcd nos tsl* (*bnt*) embryos lacking all AP patterning, the early basal DV asymmetry is similar

to WT, with only slightly reduced myosin asymmetries and dorsal movement (Fig 4b, Fig S1). At later stages, however, anisotropy of the apical myosin pool remains low and comparable to pre-VF WT levels. This result is expected given the uniform expression of pair-rule genes in a *bnt* genetic background(Blankenship et al., 2006) (Fig 4c). Consistent with these myosin distributions, we see the early dorsal flow associated with basal myosin asymmetry but a failure to produce the complex later flow patterns with their characteristic saddles and vortices. On a quantitative level our model's predictive power for AP patterning deficient *bnt* mutant embryos is comparable to WT and *twi* mutants (Fig 4a).

In summary, we have presented a simple biophysical model of morphogenetic flow that quantitatively describes complex tissue motion in terms of a hydrodynamic equation parameterized by two effective viscosities. The flow is driven by the stress defined by a linear superposition of the spatial distributions of two myosin pools. We propose that the basal myosin pool forms

an isotropic and contiguous network (He et al., 2016), contracting in a similar fashion as purified actomyosin gels in vitro(Alvarado et al., 2013; Bendix et al., 2008). Imbalance within this network, caused by the *twi* dependent depletion of myosin on the ventral side, drives global dorsal-ward flow in the pre-VF phase, which continues to contribute until early GBE (Fig 4d). Interestingly, the local depletion (on the ventral side) has a global effect, most evidently manifested by a 'sink' on the dorsal side. The apical pool decomposes into isotropic and anisotropic components. In addition to previously described accumulation of isotropic myosin in ventral regions(Martin et al., 2009), we observe a striking gradient of anisotropic apical myosin along the DV axis, reaching highest levels in lateral ectoderm and lowest levels in amnioserosa tissue at the dorsal pole. Because the force driving the flow arises from the non-uniformity of the stress, this modulation of myosin distribution is critical for the dynamics. While local rate of cell intercalation is often interpreted in terms of local myosin distribution on cellular and sub-cellular scales, our model shows that the local rate of strain is a result of the tissue-wide distribution of forces generated by the spatial non-uniformity of myosin (mathematically described by the divergence of the myosin tensor). The importance of spatial modulation (Fig 4d) suggests a novel role of the dorsal signaling pathway in generation of GBE flow. Surprisingly, in *twi* mutants both rate of increase as well as peak myosin anisotropy are significantly reduced in the first 20 minutes of GBE flow (Fig 4c). The reduced intercalation and strain rates observed in these mutants has been previously reported(Butler et al., 2009), and interpreted in terms of possible generation of AP forces by the internalized VF (absent in *twi* mutants). Our model accounts for the reduced rate of strain in terms of the changes in spatial distribution and the reduced level of myosin anisotropy. This however brings up the question of how elimination of *twi* expression in the ventral mesoderm affects myosin anisotropy in the lateral ectoderm. We suggest that this effect may be due to mechanical feedback on myosin recruitment, which relates the later to local rate of strain. Through this 'dynamic recruitment' effect (Fernandez-Gonzalez et al., 2009; Noll et al., 2015), changes in the ventral region that modify global flow patterns can affect myosin distribution and anisotropy in the lateral region. In this way, local modification of the myosin pattern can produce not only a non-local perturbation of the flow, but also a non-local perturbation of myosin distribution. The global nature of the flow is reinforced by the observed transition towards areal incompressibility at the onset of GBE-flow, which together with reduced polarization kinetics and reduced strain rates observed in *twi* mutants, indicates that non-local consequences of stress generated largely in lateral ectoderm can account for the dorsal movement of the posterior midgut.

Taken together, our observations show that morphogenetic flow is a global response to local forcing which arises from the spatial modulation of myosin density and anisotropy. The latter is derived from the spatial patterns of developmental transcription factors, but we suggest may also involve mechanical feedback affecting recruitment of myosin. Our quantitative approach provides a framework for integrating the effect of local factors in the description of the global flow.

Material and Methods

Fly lines: His2Av-mCherry(Krzic et al., 2012), Eve-YFP(Ludwig et al., 2011), $bcd^{e1}nos^{bn}tsl^4/TM3$, *halo* twi^{ID96}/Cyo (twi^{ID96} is also known as twi^1), *sqh-GFPklar*^{1}, OregonR. Embryos where dechorionated following standard procedures, and mounted in agarose gels as previously described(Krzic et al., 2012). See SI for detail on imaging setup; data pre-processing; measurements of flow field and myosin distribution/anisotropy; model and implementation.

References

R. J. Adrian. Twenty years of particle image velocimetry. *Experiments in fluids*, 2005.

B. Aigouy, R. Farhadifar, D. B. Staple, A. Sagner, J.-C. Röper, F. Jülicher, and S. Eaton. Cell Flow Reorients the Axis of Planar Polarity in the Wing Epithelium of Drosophila. *Cell*, 142(5):773–786, Sept. 2010. doi: 10.1016/j.cell.2010.07.042.

J. Alvarado, M. Sheinman, A. Sharma, F. MacKintosh, and K. Gijsje. Molecular motors robustly drive active gels to a critically connected state. *Nature Physics*, 9(9):591–597, Aug. 2013. doi: 10.1038/nphys2715.

K. Bambardekar, R. Clément, O. Blanc, C. Chardès, and P.-F. Lenne. Direct laser manipulation reveals the mechanics of cell contacts in vivo. *Proceedings of the National Academy of Sciences*, 112(5):1416–1421, Feb. 2015. doi: 10.1073/pnas.1418732112.

P. M. Bendix, G. H. Koenderink, D. Cuvelier, Z. Dogic, B. N. Koeleman, W. M. Brieher, C. M. Field, L. Mahadevan, and D. A. Weitz. A Quantitative Analysis of Contractility in Active Cytoskeletal Protein Networks. *Biophysical Journal*, 94(8):3126–3136, Apr. 2008. doi: 10.1529/biophysj.107.117960.

C. Bertet, L. Sulak, and T. Lecuit. Myosin-dependent junction remodelling controls planar cell intercalation and axis elongation. *Nature*, 2004. doi: 10.1038/nature02581.

G. B. Blanchard, A. J. Kabla, N. L. Schultz, L. C. Butler, B. Sanson, N. Gorfinkiel, L. Mahadevan, and R. J. Adams. Tissue tectonics: morphogenetic strain rates, cell shape change and intercalation. *Nature Publishing Group*, 6(6): 458–464, June 2009. doi: 10.1038/nmeth.1327.

J. T. Blankenship, S. T. Backovic, J. S. P. Sanny, O. Weitz, and J. A. Zallen. Multicellular Rosette Formation Links Planar Cell Polarity to Tissue Morphogenesis. *Developmental Cell*, 11(4):459–470, Oct. 2006. doi: 10.1016/j.devcel. 2006.09.007.

F. Bosveld, I. Bonnet, B. Guirao, S. Tlili, Z. Wang, A. Petitalot, R. Marchand, P.-L. Bardet, P. Marcq, F. Graner, and Y. Bellaiche. Mechanical control of morphogenesis by Fat/Dachsous/Four-jointed planar cell polarity pathway. *Science*, 336(6082):724–727, May 2012. doi: 10.1126/ science.1221071.

G. W. Brodland, V. Conte, and P. G. Cranston. Video force microscopy reveals the mechanics of ventral furrow invagination in Drosophila. In *Proceedings of the National Academy of Sciences*, 2010. doi: 10.1073/pnas.1006591107/ -/DCSupplemental/pnas.1006591107_SI.pdf.

L. C. Butler, G. B. Blanchard, A. J. Kabla, N. J. Lawrence, D. P. Welchman, L. Mahadevan, R. J. Adams, and B. Sanson. Cell shape changes indicate a role for extrinsic tensile forces in Drosophila germ-band extension. *Nature Publishing Group*, 11(7):859–864, June 2009. doi: 10.1038/ ncb1894.

P. Cignoni. MeshLab: an Open-Source Mesh Processing Tool. *Sixth Eurographics Italian Chapter Conference*, pages 129–13, 2010.

C. Collinet, M. Rauzi, P.-F. Lenne, and T. Lecuit. Local and tissue-scale forces drive oriented junction growth during tissue extension. *Nature Cell Biology*, 17(10):1247–1258, Sept. 2015. doi: 10.1038/ncb3226.

A. D. Edelstein, M. A. Tsuchida, N. Amodaj, H. Pinkard, R. D. Vale, and N. Stuurman. Advanced methods of microscope control using μManager software. *Journal of Biological Methods*, 1(2):10–10, July 2014.

R. Etournay, M. Popović, M. Merkel, A. Nandi, and C. Blasse. Interplay of cell dynamics and epithelial tension during morphogenesis of the Drosophila pupal wing. *eLife*, 2015. doi: 10.7554/eLife.07090.001.

R. Fernandez-Gonzalez, S. de Matos Simoes, J.-C. Röper, S. Eaton, and J. A. Zallen. Myosin II Dynamics Are Regulated by Tension in Intercalating Cells. *Developmental Cell*, 17(5):736–743, Nov. 2009. doi: 10.1016/j.devcel.2009. 09.003.

B. He, A. Martin, and E. Wieschaus. Flow-dependent myosin recruitment during Drosophilacellularization requires zygotic dunkactivity. *Development*, 143(13):2417–2430, July 2016. doi: 10.1242/dev.131334.

I. Heemskerk and S. J. Streichan. Tissue cartography: compressing bio-image data by dimensional reduction. *Nature Methods*, 12(12):1139–1142, Nov. 2015. doi: 10.1038/ nmeth.3648.

K. D. Irvine and E. Wieschaus. Cell intercalation during Drosophila germband extension and its regulation by pair-rule segmentation genes. *Development*, 120(4):827–841, Apr. 1994.

S. Klein, M. Staring, K. Murphy, M. A. Viergever, and J. P. W. Pluim. elastix: a toolbox for intensity-based medi-cal image registration. *IEEE transactions on medical imaging*, 29(1):196–205, Jan. 2010.

U. Krzic, S. Gunther, T. E. Saunders, S. J. Streichan, and L. Hufnagel. Multiview light-sheet microscope for rapid in toto imaging. *Nature Publishing Group*, 9(7):730–733, June 2012. doi: 10.1038/nmeth.2064.

C. D. Kuglin. The phase correlation image alignment method. *Proc. Int. Conf. on Cybernetics and Society, 1975*, pages 163–165, 1975.

L. D. Landau, L. P. Pitaevskii, A. M. Kosevich, and E. M. Lifshitz. *Theory of Elasticity*. Elsevier, Dec. 2012. ISBN 0080570690.

M. Z. Ludwig, Manu, R. Kittler, K. P. White, and M. Kreitman. Consequences of Eukaryotic Enhancer Architecture for Gene Expression Dynamics, Development, and Fitness. *PLoS Genet*, 7(11):e1002364, Nov. 2011. doi: 10.1371/journal.pgen.1002364.

C. M. Lye, G. B. Blanchard, H. W. Naylor, L. Muresan, J. Huisken, R. J. Adams, and B. Sanson. Mechanical Coupling between Endoderm Invagination and Axis Extension in Drosophila. *PLOS Biology*, 13(11):e1002292–27, Nov. 2015. doi: 10.1371/journal.pbio.1002292.

M. C. Marchetti, J.-F. Joanny, and S. Ramaswamy. Hydrodynamics of soft active matter. *Reviews of Modern Physics*, 2013. doi: 10.1103/RevModPhys.85.1143.

A. C. Martin, M. Kaschube, and E. F. Wieschaus. Pulsed contractions of an actin-myosin network drive apical constriction. *Nature*, 457(7228):495–501, Jan. 2009. doi: 10.1038/nature07522.

P. C. Martin, O. Parodi, and P. S. Pershan. Unified hydrodynamic theory for crystals, liquid crystals, and normal fluids. *Physical Review A*, 6(6):2401–2420, 1972. doi: 10.1103/PhysRevA.6.2401.

P. T. Merrill, D. Sweeton, and E. Wieschaus. Requirements for autosomal gene activity during precellular stages of Drosophila melanogaster. *Development*, 104(3):495–509, Nov. 1988.

K. G. Miller, C. M. Field, and B. M. Alberts. Actin-binding proteins from Drosophila embryos: a complex network of interacting proteins detected by F-actin affinity chromatography. *The Journal of Cell Biology*, 109(6 Pt 1):2963–2975, Dec. 1989.

N. Noll, M. Mani, I. Heemskerk, S. Streichan, and B. I. Shraiman. Active Tension Network model reveals an exotic mechanical state realized in epithelial tissues. *arXiv.org*, Aug. 2015.

O. Polyakov, B. He, M. Swan, J. W. Shaevitz, M. Kaschube, and E. Wieschaus. Passive Mechanical Forces Control Cell-Shape Change during Drosophila Ventral Furrow Formation. *Biophysj*, 107(4):998–1010, Aug. 2014. doi: 10.1016/ j.bpj.2014.07.013.

J. Prost, F. Jülicher, and J.-F. Joanny. Active gel physics. *Nature Physics*, 2015. doi: 10.1038/nphys3224.

J. Radon. Über die Bestimmung von Funktionen durch ihre Integralwerte längs gewisser Mannigfaltigkeiten. *Sächsiche Akademie der Wissenschaften*, 1917.

M. Rauzi, U. Krzic, T. E. Saunders, M. Krajnc, P. Ziherl, L. Hufnagel, and M. Leptin. Embryo-scale tissue mechanics during Drosophila gastrulation movements. *Nature Communications*, 6:8677, Oct. 2015. doi: 10.1038/ncomms9677.

W. L. Rickoll and S. J. Counce. Morphogenesis in the embryo ofDrosophila melanogaster—Germ band extension. *Wilhelm Roux's archives of developmental Biology*, 188(3):163–

177, 1980. doi: 10.1007/BF00849045.

A. Royou, W. Sullivan, and R. Karess. Cortical recruitment of nonmuscle myosin II in early syncytial Drosophila embryos: its role in nuclear axial expansion and its regulation by Cdc2 activity. *The Journal of Cell Biology*, 158(1):127–137, July 2002.

P. Soille. *Morphological Image Analysis: Principles and Applications*. Springer-verlag, 1999.

A. M. Sokac and E. Wieschaus. Zygotically controlled F-actin establishes cortical compartments to stabilize furrows during Drosophila cellularization. *Journal of Cell Science*, 121(11):1815–1824, May 2008. doi: 10.1242/jcs.025171.

R. Tomer, K. Khairy, F. Amat, and P. J. Keller. Quantitative high-speed imaging of entire developing embryos with simultaneous multiview light-sheet microscopy. *Nature Methods*, 9(7):755–763, June 2012. doi: 10.1038/nmeth.2062.

S. Walker. FELICITY: Finite ELement Implementation and Computation Interface Tool for You, GitHub 2014.

R. M. Warn, B. Bullard, and R. Magrath. Changes in the distribution of cortical myosin during the cellularization of the Drosophila embryo. *Journal of embryology and experimental morphology*, 57:167–176, June 1980.

J. A. Zallen and E. Wieschaus. Patterned gene expression directs bipolar planar polarity in Drosophila. *Developmental Cell*, 6(3):343–355, 2004. doi: 10.1016/S1534-5807(04)00060-7.

Supplementary Information

I. IMAGING SETUP, OPERATION, AND DATA PRE-PROCESSING
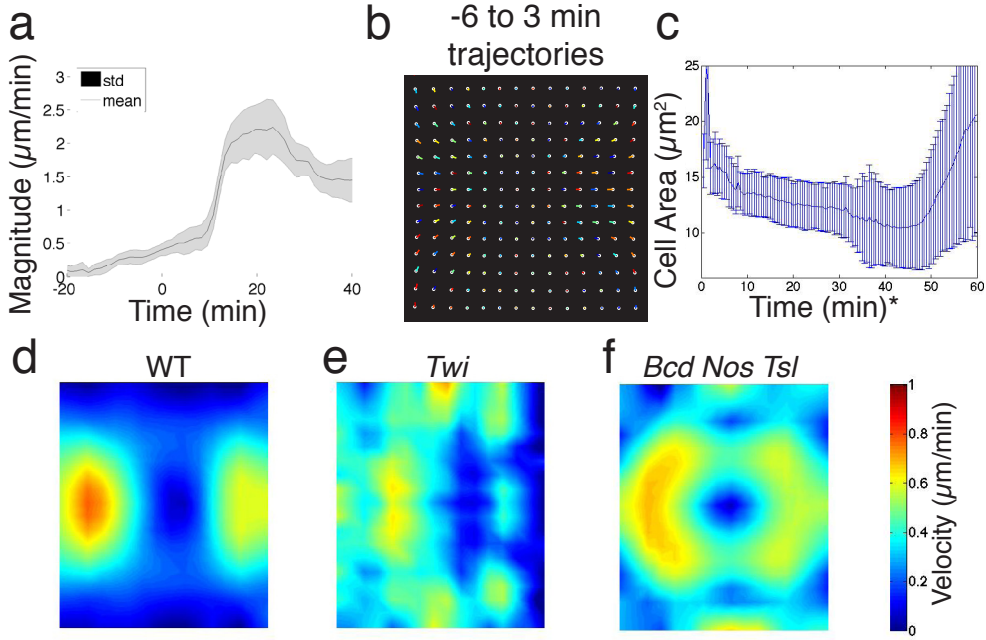
A. Light sheet microscopy

Fluorescence based live-imaging was carried out on a MuVI SPIM (Krzic et al., 2012). Briefly, the optics consisted of two detection and illumination arms. Each detection arm forms a water-dipping epifluorescence microscope, consisting of an objective (Apo LWD $25x$, NA 1.1, Nikon Instruments Inc.), a filter wheel (HS-1032, Finger Lakes Instrumentation LLC), with emission filters (BLP01-488R-25, BLP02-561R-25, Semrock Inc.), tube lens (200 mm, Nikon Instruments Inc.), and a sCMOS camera (Zyla 4.2, Andor Technology plc.), with an effective pixel size of $0.26\mu m$. Each illumination arm consisted of a water-dipping objective (CFI Plan Fluor $10x$, NA 0.3), a tube lens (200 mm, both Nikon Instruments Inc.), a scan lens (S4LFT0061/065, Sill optics GmbH and Co. KG), and a galvanometric scanner (6215h, Cambridge Technology Inc.), fed by lasers (06-MLD 488nm, Cobolt AB, and 561LS OBIS 561nm, Coherent Inc.). Optical sectioning is achieved by translating the sample using a linear piezo stage (P-629.1cd with E-753 controller), sample rotation is performed with a rotational piezo stage (U-628.03 with C-867 controller) and a linear actuator (M-231.17 with C-863 controller, all Physik Instrumente GmbH and Co. KG).

B. Experiment control and data fusion

Stages and cameras are controlled using Micro Manager (Edelstein et al., 2014), to coordinate time-lapse experiments, running on a Super Micro $7047GR - TF$ Server, with 12 Core Intel Xeon 2.5 GHz, 64 GB PC3 RAM, and hardware Raid 0 with 7 2.0 TB SATA hard drives. Samples were recorded from two, by 90^0 rotated views, at a typical optical sectioning of $1\mu m$, and temporal resolution of $75s$. As previously described (Krzic et al., 2012), MuVI SPIM optical stability allows a fusion strategy based on a diagnostic specimen. Recorded once per experiment, the diagnostic specimen is used to determine an initial guess for an affine transformation, which we feed into a rigid image registration algorithm (Klein et al., 2010), to fuse individual views, resulting in an isotropic resolution of $.26\mu m$ in the registered image.

C. Surface of Interest extraction

We used tissue cartography to extract surfaces of interest (SOI) from embryos(Heemskerk and Streichan, 2015).

FIG. S1: (a) WT ensemble averaged flow field magnitude, averaged over embryo surface. Standard deviation is across samples. **(b)** Pseudo-colored flow lines of WT embryos -6 before to 3 min past CF formation. **(c)** Cell area on the dorsal side of the embryo shrinks with time (measured using confocal microscope). $*$ indicates time starts from beginning of the experiment, at a time point during cellularization. **(d-f)** Time average length of flow lines for WT (d), *twist*, and (f) *bcd nos tsl* embryos, at times indicated in (b).

Briefly we identify the outline of the sample using the Ilastik detector to determine a point cloud for SOI construction. In a fitting step (implemented in the sphere-like fitter), we create a smooth description of the SOI in terms of cylinder coordinates defined by AP axis and azimuth (Heemskerk and Streichan, 2015). Image intensity data is then projected onto a nested group of 5 layers (2 normally evolved layers above and below the SOI), each 3 pixels apart, defining a $3 - 4\mu m$ thick 'curved image stack'. For analysis the maximum intensity projection of nested layers was used. Although the shape of embryos of the same genotype is highly reproducible, small differences in the underlying point cloud can result in small differences of the SOI passing through the apical cell surface. To simplify comparison between embryos, we create a standard projection on a cylinder grid of fixed size, with the embryo surface oriented such that apical is left, posterior right, dorsal in the centre, and ventral on top and bottom (main text Fig 1). Systematic distortions of measurements due to projecting the curved embryo surface to the plane are corrected using the metric tensor (Heemskerk and Streichan, 2015).

The apical surface is static, while the dynamic basal cell surface moves with the cellularization front. Projections of the latter could be created by reading signal on a surface obtained by evolving the apical SOI along its normal basal wards. However, small differences in cell height ($< 10\%$ of a typical cell height, and $\sim 1\%$ of the embryo diameter), could result in small but systematic bias of the SOI around the cellularization front and impair projection quality. We avoid this problem by determining a new point cloud for each time point, for which we focus the ilastik detector on the interface between basal myosin and yolk. Our model approximates the embryo as a thin shell (see below), and hence as a 2D surface. Therefore we map the dynamic basal cell surface onto the the standard cylinder grid for the static apical SOI.

II. FLOW FIELD QUANTIFICATION

A. Particle Image Velocimetry

We measure the flow field using the particle image velocimetry (PIV) method, that identifies local displacements between two time points(Adrian, 2005). Briefly, we implemented the phase correlation method that leverages favorable execution times of fast fourier transforms, to estimate local flow in a region of interest on the projections (Kuglin, 1975). To minimize effect from systematic distortions towards polar regions on cylinder projections, we adjust the size of the ROI according to the local metric strain, which we define as the deflation of the metric from flat space(Heemskerk and Streichan, 2015).

B. Reproducibility of the morphogenetic flow

Although gastrulation in *Drosophila* is highly reproducible from embryo to embryo(Irvine and Wieschaus, 1994), in practical terms experiments are subject to a constant time shift, depending on the developmental stage of the sample at the start of imaging. Thus we developed an automated routine that allowed us to identify a common time frame that the 36 (WT: $N = 22$, *twist*:7, *bcd nos tsl*:7) live-imaged embryos are registered to. Specifically, we introduced a constant time shift for a given flow field, that minimizes the squared difference with respect to a reference flow field averaged over the embryo surface:

$$\min_{t_{off,i}} \int \langle \sqrt{(\vec{v}_{ref}(t) - \vec{v}_i(t - t_{off,i}))^2} \rangle_{embryo} dt$$

, where $\langle \rangle_{embryo}$ denotes averaging across the embryo, $\vec{v}_{ref}$ is an arbitrary chosen reference from the ensemble, and $\vec{v}_i$, $t_{off,i}$ denote the i-th flow field and offset time respectively. In this way, we align samples to a chosen reference, in which we use the first occurrence of the cephalic furrow (CF) as a landmark indicating our choice for $t = 0$ min. Within a given genotype, we could automatically determine the offset time. However, to align mutants to WT, we first aligned all mutant datasets, and then used landmarks such as the CF (*twist*), or the VF(*bcd nos tsp*), to define a common time frame as best as we can.

Time shifted accordingly, we created an ensemble average flow field for each genotype:

$$\langle \vec{v} \rangle_{ensemble}(t) := \frac{1}{N} \sum_i^N \vec{v}_i(t - t_{off,i})$$

The magnitude of ensemble average is highly reproducible from embryo to embryo (note the small standard deviation, Fig S1a). Flow trajectories during cellularization point towards the dorsal side (Fig S1b), showing persistent movement towards dorsal regions during pre-CF flow. This is accompanied by reduction of apical cell area in these regions (Fig S1c), as measured using confocal microscopy. While the length of pre-VF flow lines peaks on the anterior and posterior poles in WT, it is substantially reduced near poles in *twist*, and only mildly reduced in *bcd nos tsl* (Fig S1d-f). Together with the loss of basal DV asymmetry this suggests that *twist* mediated reduction of basal myosin levels on the ventral side is responsible for dorsal-ward flow.

III. MYOSIN QUANTIFICATION

A. Intensity normalization

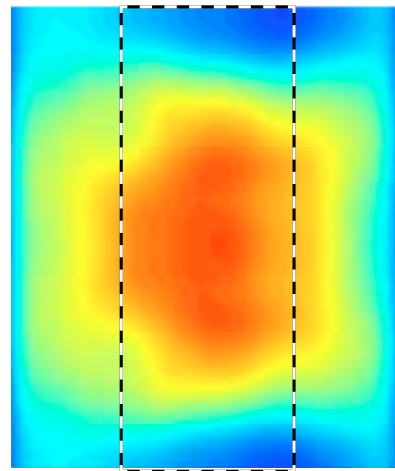Using the imaging and pre-processing procedure as outlined above with samples expressing sqhGFP (Royou et al., 2002), we created projections of the apical and basal cell surfaces, with the goal of establishing a quantitative measurement of global myosin patterns. Ideally, quantification of signal intensities is carried out using identical conditions for each sample in the pool used for statistics, to minimize variability across samples. However, when performing *in toto* live-imaging, it is difficult to image more than one sample at a time and keep a high recording frequency. To minimize variability in a sequential recording scheme, we keep imaging conditions constant, but there are still possible variabilities in recorded signal intensity for biological but also technical reasons.

To account for such variability between experiments, we normalize recorded data. Signal intensity of all time points in a given experiment are summarized by normalizing the intensity distribution: upper and lower range are determined according to the $ll = 0$ and $ul = 80$-percentile; normalization is done by subtracting the ll and dividing by ul, yielding a dimensionless normalized signal distribution. This strategy should not only allow for comparison on the same microscope, but also across microscopes, allowing for validation of *in toto* live-imaging from sequential experiments against fixed batches imaged e.g. on a confocal.
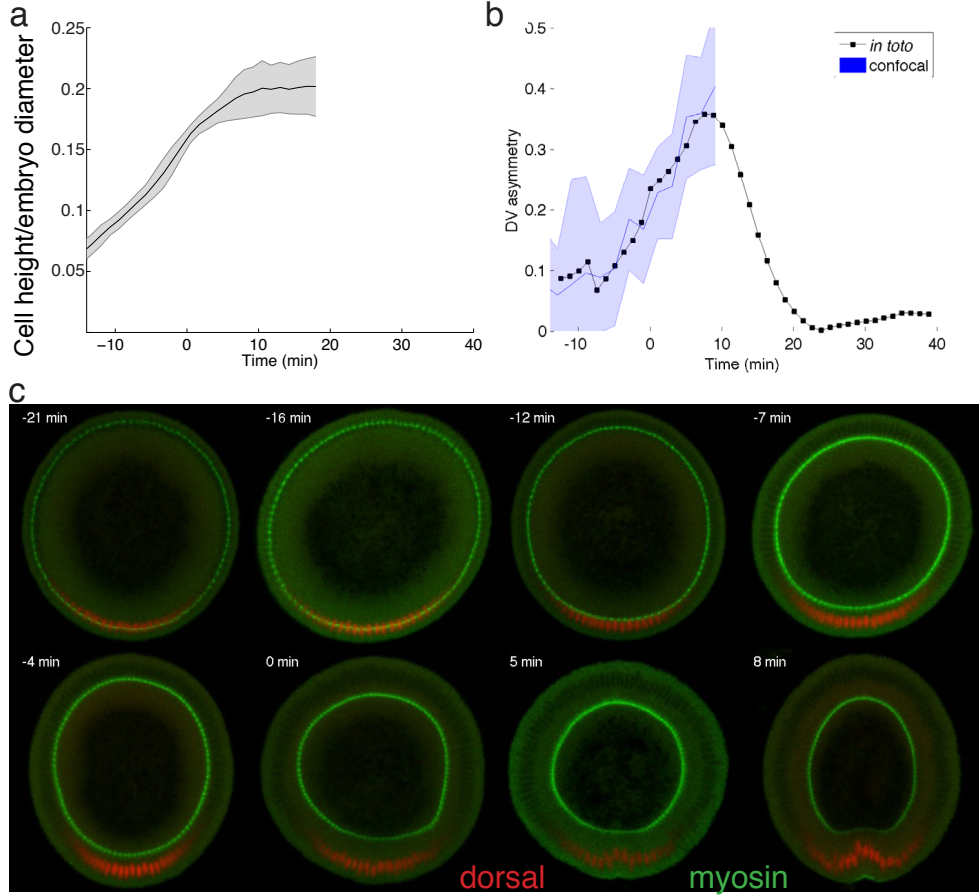
B. Basal myosin pool analysis

1. Basal myosin pool via Light Sheet Microscopy

Here we briefly outline the results for the DV asymmetry in the basal myosin pool that we reported in the main text. First, we time align intensity normalized basal projections as described above. Next we convolve each pullback with a gaussian of width $\sigma \sim 3$ cell diameters to obtain basal myosin at the mesoscale (see discussion in model section below for definition). The results are then ensemble averaged to obtain ensemble myosin distribu-

FIG. S2: Basal myosin, (as main text Fig 1g). Dashed box indicates region used to evaluate DV asymmetry.

FIG. S3: Basal myosin light sheet versus confocal. **(a)** Cell height as a function of embryo diameter increases monotonically until ventral furrow formation starts. **(b)** DV asymmetry as a function of time, measured using light sheet (black), or confocal with time calibration curve according to cell height (blue). **(c)** Confocal recording of DV cross sections of embryos cut along AP axis. Colors indicate localization of myosin and dorsal visualized via antibody stainings. Embryos were fixed by heat-methanol fixation (Miller et al., 1989) for staining with mouse anti-Dorsal ($1:50$, $7A4 - S$ Developmental Studies Hybridoma Bank (DSHB)] and rabbit anti-myosin II (Zipper heavy chain, $1:1000$, (Sokac and Wieschaus, 2008)). Secondary antibodies coupled to Alexa Fluor 488 and Alexa Fluor 564 were used at a $1:500$ dilution (Invitrogen).

tion as shown in Fig. S2. To assess DV asymmetry, we focus on the region outlined by the black/white dashed line, where we first take an average along the AP axis and then compute average signal on dorsal side, and subtract from it the average signal on the ventral side. Repeating the outlined routine for all time points, we obtain the plot show in main text Fig 4b.

2. Basal myosin pool via Confocal Microscopy

Fig. S3c shows DV cross sections of fixed embryos stained for rb anti zipper and mouse anti dorsal, cut along the AP axis, and imaged on a confocal microscope. DV orientation of the samples is automatically determined based on the dorsal signal. To estimate the age of fixed embryos in relation to live-imaging data, we constructed a calibration curve for cell apico-basal height shown in Fig S3a. Using the known monotonic relation between

cell height and age(Merrill et al., 1988), which we find lasts until about $8min$ after CF formation, we obtain estimate for the age of a fixed embryo based on measuring cell height. By segmenting the outline of basal myosin, we can then measure DV asymmetry in the same way as described for live-imaging data above.

A direct comparison between live-imaging based DV asymmetry measurement, and based on $N = 345$ fixed DV cross sections from confocal shows that after applying normalization routine as described above, we find similar estimates for the DV asymmetry using both light sheet and confocal imaging (see Fig S3b). Not that uncertainties in the calibration curve propagate to exact age determination in the embryo, and thus increased fluctuations in DV asymmetry determined using confocal imaging.

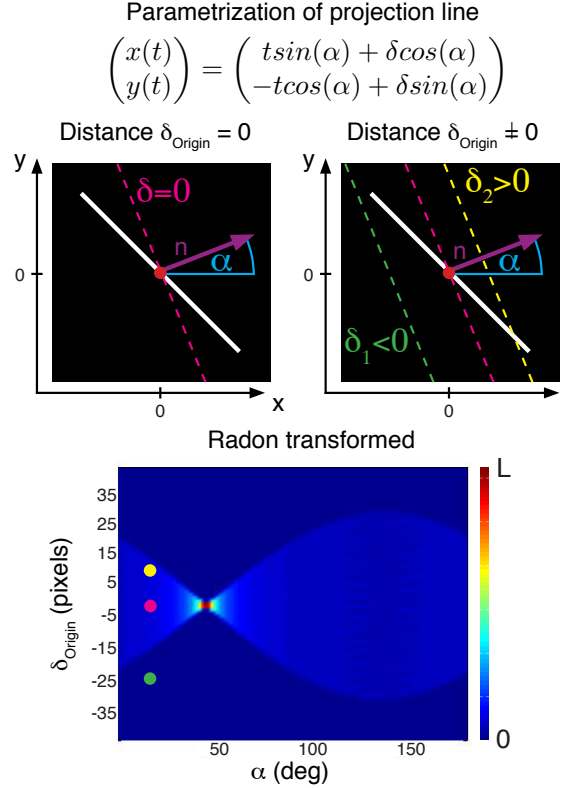## C. Segmentation free anisotropy detection using Radon transforms

When viewed in cross-section, the cell cortex in epithelia forms a polygon tiling, where the outline of each cell is well approximated by a closed sequence of edges. Anisotropic distribution of proteins is often characterized by homogeneously increased accumulation to cell edges of particular orientation, while it remains homogeneously low and comparable to background on other edges(Zallen and Wieschaus, 2004)(Blankenship et al., 2006)(Bertet et al., 2004). Note that typically the number of edges at low and high signal accumulation are roughly equal. Available methods to quantify cortical anisotropy mostly operate at the single cell level and construct a nematic tensor by integrating signal intensities along cell outlines(Aigouy et al., 2010). At the organismal scale membrane segmentation is costly, and for polarized markers low signal to noise on a significant number of edges often results in difficulties to close the cell circumference. We overcome the need for fiduciary markers that increase experiment complexity, by shifting perspective to cell edges and designing a robust and rapid segmentation free anisotropy detection algorithm.

Let's consider an image on a rectangular domain Ω, showing an edge of possibly non-uniform intensity, assigning each pixel at coordinates $(x, y) \in \Omega \subset \mathbb{R}^2$ some intensity $I(x, y) \in \mathbb{R}$ - as shown e.g. in Fig S4. Lets call this edge a **linear signal** or just signal. For simplicity, and without loss of generality, we assume the average intensity along the linear signal is $< I_{ls} >= 1$, and average background intensity is $< I_{bg} >= 0$. While under favorable conditions with high signal to noise ratio, it may be possible to identify the linear signal using conventional methods such as edge detection using a typical threshold, this task will be substantially more error prone at low signal to noise ratio.

Therefore, we decided to reformulate the problem using radon transforms (Radon, 1917), that integrate signal along lines of a given angle and signed distance from the origin. Consider a line L with normal $\mathbf{n_L} = (cos(\alpha), sin(\alpha))$, a signed normal distance $\delta \in \{-\infty, \infty\}$ away from the origin (e.g. shown in pink in Fig S4, top left), which may be parametrized as follows

$$\begin{pmatrix} x(t) \\ y(t) \end{pmatrix} = \begin{pmatrix} tsin(\alpha) + \delta cos(\alpha) \\ -tcos(\alpha) + \delta sin(\alpha) \end{pmatrix} \quad (1)$$

, where $t \in \{0, 1\}$ is the parameter that marks position along the line L (Fig S4). It is clear that all possible pairs of normal orientation and signed distance (α, δ), describes all possible lines covering the plane. The **radon transform** of the image I - denoted $\mathcal{R}I$ - establishes a map from the rectangular domain Ω, on which the image is defined into the space spanned by line orientation and signed distance, where each line L characterized by the pair (α, δ) is assigned the integrated(summed) intensity
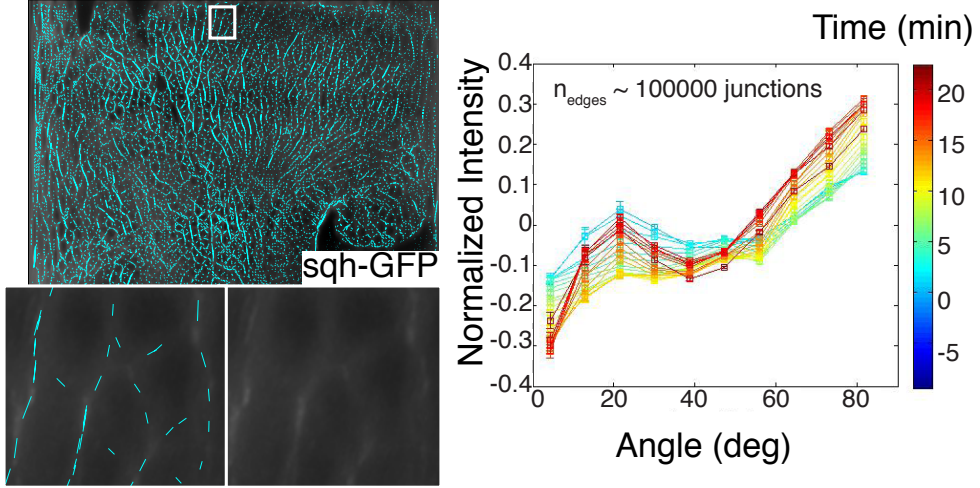
Parametrization of projection line

$$\begin{pmatrix} x(t) \\ y(t) \end{pmatrix} = \begin{pmatrix} tsin(\alpha) + \delta cos(\alpha) \\ -tcos(\alpha) + \delta sin(\alpha) \end{pmatrix}$$

FIG. S4: Illustration of how to construct a radon transform for an image with constant background $I = 0$, shown in black and foreground $I = 1$, shown in white (top), and resulting radon transform (bottom). Colors indicate different lines, and the result in the radon transform is indicated as colored circle.

projection along the line - or in mathematical terms:

$$\mathcal{R}I(L) = \int_L I(x, y) d\Omega$$

$$\mathcal{R}I(\alpha, \delta) = \int_0^1 I(tsin(\alpha) + \delta cos(\alpha), -tcos(\alpha) + \delta sin(\alpha)) dt$$

, where the latter equation uses the explicit parametrization of the line L in terms of α, δ, t defined above. (The following is a verbal example for the equation above, and may be skipped): Fig S4 illustrates the algorithm that constructs the radon transform for the linear signal shown in white, that has a normal orientation of 45^0 and constant intensity $I_{ls} = 1$ over a background of intensity $I_{bg} = 0$. The magenta dashed line indicates a line L with normal orientation α and a distance $\delta = 0$ away from the origin shown in red. Integrating image intensity along such a line, for any orientation $\alpha \neq 45^0$, we theoretically obtain only a contribution from the intersection with the linear signal, thus $\mathcal{R}I(\alpha \neq 45^0, 0) = 1$. In contrast for $\alpha = 45^0$, i.e. when the line is parallel and on top of the linear signal, the radon transform integrates the intensity along the entire line, returning the length l of the linear

FIG. S5: Example of edges identified with our anisotropy detection algorithm, and a magnification in a region of interest showing result in comparison with underlying raw data (left). Time course of normalized intensity (shifted to zero mean) versus edge orientation. Color codes for time as indicated in the colorer (right).

signal: $\mathcal{R}I(\alpha = 45^0, 0) = l$. In our example, for $\delta \neq 0$ we will either have a single intersection of the line L with the signal, again returning with the same outcome as above, or no intersection, where the radon transform returns 0, indicated by the dark blue regions in Fig S4.

Since the radon transform is linear, it follows that for any image that is the linear superposition of linear signals, the radon transform is the linear superposition of the radon transform of each linear signal. For example, if an image consisted of 2 linear signals (for example a four fold vertex), the resulting radon transform is the sum of the radon transform of each linear signal, with peak levels at orientation and signed distance of each linear signal. In this way, linear signals are mapped to peaks in the radon transform that reflect the total intensity along the length of the linear signal. Knowing the location of peaks in the radon transformed space allows us to reconstruct the position and orientation of each linear signal in the image. This simplifies the task of identifying the linear signal, as detection of peaks due to their compact structure is simpler than detection of edges, and the radon transformed signal will be less susceptible to fluctuations in the underlying data, and therefore enhance robustness.

To obtain average image intensity from the radon transform we use that the height of the peak reflects the total intensity I_{tot} along the linear signal, to construct the average signal as

$$< I > = I_{tot}/l$$

where l denotes the length of the linear signal. To determine the length of the linear signal, we need to determine the position of where the linear signal begins and/or ends in the image. This is done by interpolating the signal along the orientation and position corresponding to the identified peak in the radon transform, and identifying discontinuities in the interpolated signal, which mark

the boundaries of the linear signal. With beginning and end determined, we obtain the length as the magnitude of the vector connecting the two points. If beginning and end don't fall onto the boundary of the image, we perform an integration of a line restricted between these two endpoints, to obtain a more accurate estimate of the total line intensity.

D. Validation of segmentation free anisotropy detection

Pullbacks created with ImSAnE based on light sheet microscopy data of developing *Drosophila melanogaster* embryos show the cortex of roughly 6000 cells, which would yield a complex radon transform pattern, effectively impeding peak detection. To simplify peak detection, we decided to carry out analysis in small blocks, where we focus on a local region of interest (ROI) that we sweep across the entire image. The size of the local region is chosen such that it can accommodate between $1-3$ typical edge lengths l_{edge}. In this way, we typically obtain a small number (< 10) of edges in the ROI, such that we could use the extended-maxima transform(Soille, 1999) to identify the typically well separated peaks. To avoid double counting of edges - as they may appear from sweeping the ROI - we average detected lines of locally similar angles with a small angular difference $\|\delta_\alpha\| < \epsilon$ and distance $\delta < l_{edge}$.

Following the general prescription given above, we obtain local estimates for position, orientation, and average intensities of cell edges, demonstrated in Fig S5. A zoom on a local region indicated by the white box shows that this routine - fully automatically, and without need of fine tuning parameters - faithfully detects the orientation of cell edges, including dim edges with only minimally stronger signal compared to background. To

further benchmark the quality of intensity estimates, we turned to known anisotropy of myosin during germband extension (Blankenship et al., 2006). Fig S5 shows on the right, that the presented algorithm finds the normalized intensity on AP edges (90^0) is systematically higher than on DV edges (0^0), reaching is maximum approximately 20 min after cephallic furrow formation, in good agreement with previous manual measurements (Blankenship et al., 2006).

IV. MODEL OF TISSUE FLOW

A. Derivation of a mathematical model

Mechanics of epithelial tissue is largely defined by the properties of intracellular cytoskeletal cortexes, linked by cadherin mediated adherents junctions into a global trans-cellular mechanical network. This mechanical network is "active" in the sense that it involves myosin motors that generate internal forces and can do work by contracting actin-myosin filaments under tension. Cytoskeletal network is also "adaptive" in the sense that it can relax mechanical stress by reorganizing internally, on sub-cellular scale by recruiting (or releasing) myosin and other key molecular components, and on tissue scale, by allowing cells to rearrange locally (by T1 processes). The latter process allows cells to change neighbors and "flow" relative to each other, while preserving the integrity of the epithelium and its cytoskeletal network. Yet, the detailed description of these complex cellular processes is not necessary for our present goals, which call merely for an approximate mesoscale description of tissue mechanics. By mesoscale we mean the scale of 3-10 cell diameters, still much smaller than the macroscopic scale of the embryo tissue flow. Microscopic complexity notwithstanding, on mesoscale we will think of tissue as a continuous medium and it will suffice for us to capture the facts that i) on short time scales tissue responds elastically to mechanical perturbations (Bambardekar et al., 2015) and ii) on the longer time scales elastic stress is relaxed through active rearrangement of the cytoskeleton as cells adapt to the imposed deformation. This is enough to define flow velocity in response to external and internal stress: on the timescale comparable to internal stress relaxation, tissue dynamics can be described by a generic viscoelasticity equation with two effective viscosity parameters which we shall now derive.

Short-term elastic response means that incremental increase of strain causes an increase in stress, which can subsequently relax with the relaxation time τ_R. Elastic stress is then governed by the Maxwell viscoelasticity and in the mesoscopic continuum approximation we have:

$$\dot{\sigma}_{ab} = \mu(\partial_a \dot{u}_b + \partial_b \dot{u}_a) + \lambda \delta_{ab} \partial_c \dot{u}_c - \tau_R^{-1} \sigma_{ab} \qquad (2)$$

where $\dot{x} = \frac{d}{dt} x$ so that $\dot{u}_a$ is the rate of local displacement (index a denoting the spatial component assumed to be locally tangential to the surface of the embryo). Spatial derivatives of the $\dot{u}_a$ vector define local rate of strain $\partial_a \dot{u}_b + \partial_b \dot{u}_a$. In addition, δ_{ab} is the Kronecker delta matrix and we have adopted the Einstein convention of summing over repeated indices (e.g. $\partial_c u_c = \sum_c \partial_c u_c$). The 1st two terms on the right hand side describe generation of stress in proportion to the rate of strain (μ, λ are the Lame coefficients parameterizing an elastic stress-strain relation) and the last term parameterizes relaxation of stress.

On the other hand, in the continuum approximation, tissue flow velocity $v_a = \dot{u}_a$ can be described by the (compressible) Stokes equation

$$\rho \dot{v}_a = \nu_0 \partial_b^2 v_a + \partial_b \sigma_{ab} + F_a \qquad (3)$$

where F_a is external force (per unit volume), ρ is the density and ν_0-dynamic viscosity.

Now suppose that stress relaxation is sufficiently rapid to achieve quasi-equilibrium

$$\tau_R^{-1} \sigma_{ab} \approx \mu(\partial_a v_b + \partial_b v_a) + \lambda \delta_{ab} \partial_c v_c \qquad (4)$$

substituting σ_{ab} into Eq.2 we have

$$\rho \dot{v}_a = (\nu_0 + \tau_R \mu) \partial_b^2 v_a + \tau_R(\mu + \lambda) \partial_a \partial_b v_b + F_a \qquad (5)$$

Note that transient elasticity, parameterized by τ_R, μ and λ generates "effective viscosity" $\tau_R \mu$ which can dominate the microscopic viscosity ν_0 of the "fluid" itself. This effective viscosity is in general anisotropic with $\tau_R \mu$ contributing to the shear viscosity which acts on the incompressible component of the flow and $\tau_R(2\mu + \lambda)$ which acts on the irrotational component.

If the effective viscosity is sufficiently high and flow changes sufficiently slowly, the inertial term can be neglected ($\rho \dot{v}_a \ll \nu \partial_b^2 v_a$) and the quasi-stationary flow is defined by the balance of the external forcing and effective viscosity

$$\nu \partial_b^2 v_a + \nu' \partial_a \partial_b v_b = -F_a \qquad (6)$$

where $\nu = (\nu_0 + \tau_R \mu)$ and $\nu' = \tau_R(\mu + \lambda)$. Since external force is related to external stress via $F_a = \partial_b \sigma_{ab}^{ext}$ and we have argued that relevant "external stress" that drives tissue flow in the embryo is proportional to the myosin tensor $\sigma_{ab}^{ext} \sim -m_{ab}$ we have arrived at the equation we have used in the main text to relate tissue flow velocity with myosin distribution. (Note that the minus sign in the relation of σ_{ab} and m_{ab} is due to the fact that myosin generates contractile forces, so that a local maximum of an isotropic myosin distribution $m_{ab}(r) = \delta_{ab} m(r)$ would act just like a low pressure region, generate inward directed flow.)

$$\nu \partial_b^2 v_a + \nu' \partial_a \partial_b v_b = \partial_b m_{ab} \qquad (7)$$

B. Passive versus active mechanics

In the section above we put forward a simple effect model based on conventional Maxwell viscoelasticity. Epithelial tissues however are clearly not ordinary passive

viscoelastic materials. Myosin-driven rearrangement of the cytoskeleton is an active and adaptive process, which can be regulated on cellular and subcellular scales. Yet, we argue, that average flow on mesoscopic scale can be usefully approximated by the passive viscoelastic model with suitable effective parameters. The ability of this simple model to capture highly non-trivial spatial flow patterns without the need for introducing spatial dependence of model parameters, proves the validity of the approximation. Still, we do not expect this "passive viscoelasticity" model to be complete. We anticipate that a more detailed description of myosin activity and myosin recruitment dynamics would be required in order to describe both, the fast cellular scale fluctuations and the long-term myosin dynamics on the scale of the embryo. Other molecular/genetic factors will come into play as well: e.g. cadherin and other cytoskeletal components on small scale and transcription factors that guide morphogenesis on large scales. We plan to address these issues in the future.

C. Finite element implementation using FELICITY

Inversion of the continuum equation of state relating the coarse-grained myosin tensor and cellular flow-field was achieved using Finite Element Methods (FEM) in the weak formulation implemented within the FELICITY toolbox for MATLAB (Walker, GitHub 2014). Equations were inverted on a static triangular mesh representing the 'canonical' embryo surface produced via a point cloud (described above) subsequently turned into a smooth triangulation using MeshLab (Cignoni, 2010). As such, all objects within the equation of state had to be parameterized within the 3D embedding space of the mesh, which can be done by using the direction relation between projections and SOI(Heemskerk and Streichan, 2015). The only dynamic input to this inversion algorithm is the divergence of the myosin tensor. This was computed by interpolating the gradient of each cartesian component of the tensor onto triangular faces of our mesh, producing a 3x3x3 object on each face. The partial trace of this object over directions within the tangent plane of the face result in the estimated divergence. This operation was repeated for all myosin pools used. All equations within the FEM software are projected onto the surface of our 3D mesh to manually ensure solutions only exist within the tangent plane.

In order to model internalization of the VF, we introduced the ability to add a 'cut' within the triangular mesh. Contraction of the tissue was modeled by manually introducing local force dipoles on edges within the mesh pointing along the bond. All vertices along the cut were given zero bulk modulus to allow for local tissue compression needed to simulate invagination. The location of the cut was estimated from the PIV flow fields. Specifically the ratio of the divergence of the velocity field to the velocity field's magnitude was used to estimate the spatial extent of the cut over times during ventral furrow formation.

Predictions for the flow field obtained via inversion are subject to an overall scale factor, that can't be determined by the model. To compare ensemble averaged flow field measurement $\vec{v}(t)$ to model predictions $\vec{u}(t)$ in a quantitative fashion, we define a global measure for the spatial residual that is insensitive to such a scale factor. With the short hand notation $\langle \vec{u} \rangle := \sqrt{\langle \vec{u}^2 \rangle_{embryo}}$, the residual

$$R = \frac{(\langle \vec{u} \rangle^2 \vec{v}^2 + \langle \vec{v} \rangle^2 \vec{u}^2) - 2\sqrt{\langle \vec{u} \rangle^2 \langle \vec{v} \rangle^2} \vec{v} \cdot \vec{u}}{2 \langle \vec{u} \rangle^2 \langle \vec{v} \rangle^2}$$

provides a spatial discrepancy map, indicating the prediction quality as a function of location on the embryo, that is in-sensitive to noise dominated fluctuations in domains of no flow (i.e. fixed points), as opposed to e.g. inner product.